Constraining the Properties of Milky Way Dwarf Spheroidals with Surface Brightness & Velocity Dispersion Data

Justin Craig, Casey R. Watson
Department of Physics & Astronomy, Millikin University, Decatur, IL, USA.

Introduction

Dark matter (DM) is the dominant form of matter in the universe [1]. Observations of rotation curves (Fig. 1), suggest that every galaxy is embedded within a large DM halo (Fig. 2), that comprises, on average, 84% of the mass of each galaxy and the same fraction of matter in the universe as a whole [1,2,3].

Fig. 1: Rotation curves reveal the need for extra, unseen mass in galaxies [4].

Fig. 2: DM Halo [5]

As the most DM-dominated systems in the universe, dwarf galaxies serve as excellent DM laboratories [1,2]. In this poster, we use stellar velocity dispersion and surface brightness profile data to infer the DM properties of 9 Milky Way dwarf spheroidal galaxies (dSphs).

Data and Galaxy Selection

In this work, we only consider Milky Way (MW) dSphs for which both high quality surface brightness (SB) and velocity dispersion data exist. We make further cuts based on 3 additional factors: 1. Tidal disruption, 2. Spherical Symmetry, and 3. Constraints on the inner slope, γ, of the stellar density profile, $\nu(r)$.

1. Tidal disruption

MW dSphs are often tidally disrupted by the gravitational influence of the much larger MW that they orbit, e.g., [6]. Tidal disruption disturbs the equilibrium that is assumed in the orbital analysis we will conduct, so we must discard dSphs undergoing disruption.

2. Spherical Symmetry

Due to increased and uncertain projection effects, analysis of velocity dispersion data is skewed for dSphs that are more ellipsoidal. We therefore restrict our galaxy sample to dSphs that are statistically well-described by only 1 axial radius (spherical) rather than 3 independent axial radii (ellipsoidal), according to the analysis of Ref. [7].

3. Inner profile slope

Finally, we limit our study to dSphs with uncertainties in γ of $\leq 20\%$ [7].

Based on the above criteria, we are left with the following sample of 9 dSphs that are included in this research are Canes Venatici I, Canes Venatici II, Draco, Fornax, Leo I, Leo II, Sextans, Ursa Minor, [10-11], and Reticulum II [12-13].

Constraining Mass and Velocity Anisotropy

Using the following three steps, e.g., [14-16], we constrain both the mass and velocity anisotropy profiles.

I. Surface Brightness (SB) Profile Analysis

The SB profile of a galaxy is the 2D projection of light from its 3D distribution of stars, $\nu(r)$, on the plane of the sky. Mathematically, this is given by the Abel Transform:

$$\Sigma(R) = 2\int_R^\infty \frac{\nu(r) r dr}{\sqrt{r^2 - R^2}} + \Sigma_{bd} \qquad (1)$$

where R is the observed, projected 2D radius, r is the 3D radius and Σ_{bd} is the observed background light. The observed SB profile, $\Sigma_{obs}(R)$, can be compared to Eqn. (1) for a given choice of $\nu(r)$ to determine the scale radius, R_*, that is shared by $\Sigma(R)$ and $\nu(r)$. For this study, we adopt the following form of $\nu(r)$ [7]:

$$\upsilon(r) = \frac{\nu_o}{\left(\frac{r}{R_*}\right)^\gamma \left(1+\left(\frac{r}{R_*}\right)^2\right)^{\frac{n-\gamma}{2}}} \qquad (2)$$

Ref. [7] constrained the values of γ in Eqn. (2) for a large number of MW dSphs for two values of the outer profile slope, n: n=5 (standard Plummer value [17]) and n=9 (their "steeper" profile value). Letting $y = r/R_*$ and $Y = R/R_*$, when we combine Eqns. (1) and (2), the projected stellar light profile becomes:

$$\Sigma(Y) = \Sigma_o \int_{u=0}^\infty \frac{du}{(u^2+Y^2)^{\frac{\gamma}{2}}(1+u^2+Y^2)^{\frac{n-\gamma}{2}}} + \Sigma_{bd}\,, \qquad (3)$$

where $u = \sqrt{y^2 - Y^2}$ and $\Sigma_o = 2\nu_o R_*$. Comparing Eqn. (3) to $\Sigma_{obs}(R)$, we determine the best-fit value for R_* for each of the dSphs in our sample.

Abstract

Using a combination of surface brightness and velocity dispersion data, we simultaneously constrain the velocity anisotropy and dark matter mass profiles of Milky Way dwarf spheroidals (dSphs). Our findings indicate strong correlations between the distributions of visible and dark matter within the dSphs and provide further insights into the cusp vs. core debate.

II. Spherical Jeans Equation Analysis

Given R_* and Eqn. (2), we can now use the Spherical Jeans Equation (SJE: Eqn. 4) to determine other parameters of interest [18]

$$y\sigma_r^2(y)\left(\frac{dln\sigma_r^2(y)}{dlnr} + \frac{dln\nu(y)}{dlnr} + 2\beta(y)\right) = -\sigma_0^2 I(x)\,. \qquad (4)$$

We adopt the following forms of the radial velocity dispersion profile and velocity anisotropy profile, $\sigma_r^2(y)$ and $\beta(y)$, respectively, for our analysis:

$$\sigma_r(y) = Dy^s(1+y^2)^{(t-s)/2}\,, \qquad (5)$$

where D is a normalization constant, and t and s are free parameters, and

$$\beta(y) = \frac{\beta_o + \beta_\infty y^2}{1+y^2}\,, \qquad (6)$$

where β_o and β_∞ are free parameters that describe β at the center of a dSph and at large radii, respectively [16].The coefficient σ_0^2 in Eqn. (4) is given by $\sigma_0^2 = GM_0/R_*$, where $M_0 = 4\pi\rho_{DM}{r_{DM}}^3$, ρ_{DM} and r_{DM} are, respectively, the density and scale radius parameters of the chosen DM halo model, and $x = r/r_{DM}$. The two DM density models we consider are the Burkert ($r_{DM} = r_o$; [19]) and NFW ($r_{DM} = r_s$; [20]) profiles, and the mass integrals over these profiles ($I(x)$ in Eqn. (4)) are shown in Eqns. (7) and (8).

$$I_{Burkert}(x) = \int_0^\infty \frac{x^2 dx}{(1+x)(1+x^2)},\ x = \frac{r}{r_0} \qquad (7)$$

$$I_{NFW}(x) = \int_0^\infty \frac{x^2 dx}{x(1+x)^2},\ x = \frac{r}{r_s} \qquad (8)$$

When we let $x = \alpha y$ (which also means $r_o = R_*/\alpha$ or $r_s = R_*/\alpha$), and combine Eqns. (4)-(6), we find:

$$y^{2s+1}(1+y^2)^{t-s-1}(A + By^2) = I(\alpha y)\,, \qquad (9)$$

$$\text{where}\quad A = \left(\frac{D}{\sigma_o}\right)^2[\gamma - 2(\beta_o + s)] \text{ and } B = \left(\frac{D}{\sigma_o}\right)^2[n - 2(t+\beta_\infty)]. \qquad (10)$$

The general form of Eqn. (9) is somewhat daunting because, without constraints, there are 9 free parameters: α, β_0, β_∞, D, γ, n, σ_0, s, and t. However, n and γ have been established in Ref. [7] from SB data and with the above parametrization (Eqn. 10), there are effectively only 5: α, A, B, s and t. Futher, we can consider limits of Eqn. (9) to determine realistic ranges for these parameters.

For $y \to 0$, A ~ 0 and, therefore, $\beta_o \sim \gamma/2 - s$ for both Burkert and NFW, and s ≤ 0 ($s \leq -0.5$) for the Burkert (NFW) profile, as I(x) → $x^3/3$ ($x^2/2$).

For $y \to \infty$, Eqn. (9) demands that I(x) must approach a power-law form: I(x) ~ $x^{(1+2t)}$, which it does, yielding -0.3 < t < 0 for both profiles, depending on the value of α.

When we allow A, B, s, and t to vary without restrictions between -1 and 1 for $0.5 \leq \alpha \leq 3$, we find:

1) Solutions that satisfy Eqn. (4) to within a few percent exist for A, B, s, and t for a wide range of α for the adopted forms of $\upsilon(r)$, $\sigma_r^2(y)$, and $\beta(y)$ in Eqns. (2), (5), and (6).
2) Solutions for the Burkert (NFW) profile are accurate to ≤ 3% (≤ 2%) for $1 \leq \alpha \leq 2.5$ ($0.7 \leq \alpha \leq 2.5$).
3) Minimum uncertainty A, B, s, & t are well-defined functions of α & respect all limits considered above.

With A, B, s & t known for a given α, we can use Eqn. (10) and step III (below) to find the remaining parameters: D, β_0, β_∞, and M_0. Note that constraining M_0 also determines $\sigma_0^2 = GM_0/R_*$ and the DM density parameter via $M_0 = 4\pi\rho_{DM}{r_{DM}}^3$ [$\rho_{DM} = \rho_o$ for Burkert and $\rho_{DM} = \rho_s$ for NFW].

III. Velocity Dispersion Analysis

With the results from step II, we can now use another Abel Transform (similar to step I) to determine the projected velocity dispersion [16]:

$$\sigma_p^2(Y) = \frac{2}{\Sigma(Y)}\int_{R/R_*}^\infty \left(1 - \beta(y)\left(\frac{Y}{y}\right)^2\right)\frac{\nu(y)\sigma_r^2(y)R_* dy}{\sqrt{y^2 - Y^2}}\,. \qquad (11)$$

We can then compare Eqn. (11) to the observed velocity dispersion profile data for each dSph to determine D, β_0, β_∞, and M_0. Our results are shown in Tables 1 and 2 and Figs. 3-5 in the Results section.

Results

Table 1. The star-related quantities derived from observations and steps I and II with the values for n, γ, and R_e from Ref. [7] and $\gamma_e = R_e/R_*$.

Galaxy	n	γ	γ_e	R_e/(pc)	R_*/(pc)	α (B)	α (NFW)	β_0 (B)	β_0 (NFW)	β_∞ (B)	β_∞ (NFW)	D (B)	D (NFW)
CVI	5	$0.60^{+0.08}_{-0.06}$	$0.785^{+0.050}_{-0.032}$	452 ± 13	576 ± 17	1.0 ± 0.1	0.7 ± 0.1	0.27 ± 0.05	0.97 ± 0.01	-1.51 ± 0.57	-12.15 ± 0.01	7.7 ± 2.2	3.6 ± 1.2
CVII	5	$0.53^{+0.12}_{-0.10}$	$0.756^{+0.024}_{-0.031}$	70.7 ± 11.2	93.6 ± 14.8	1.1 ± 0.1	0.9 ± 0.1	0.29 ± 0.05	0.93 ± 0.02	0.23 ± 0.20	−7.90 ± 1.16	3.5 ± 1.5	1.6 ± 0.7
Draco	9	$0.27^{+0.02}_{-0.01}$	$0.559^{+0.001}_{-0.003}$	214 ± 2	383 ± 4	1.0 ± 0.1	0.7 ± 0.1	0.11 ± 0.05	0.75 ± 0.02	-0.83 ± 0.29	−3.89 ± 0.67	8.3 ± 2.5	5.0 ± 1.0
Fornax	9	$0.27^{+0.01}_{-0.01}$	$0.504^{+0.002}_{-0.002}$	838 ± 3	1662 ± 6	1.0 ± 0.1	0.7 ± 0.1	0.11 ± 0.05	0.75 ± 0.02	0.92 ± 0.23	−3.76 ± 0.45	11.1 ± 1.1	5.9 ± 1.3
Leo I	9	$0.20^{+0.01}_{-0.01}$	$0.456^{+0.002}_{-0.001}$	270 ± 2	592 ± 4	1.2 ± 0.1	1.8 ± 0.3	0.17 ± 0.04	0.94 ± 0.05	-1.52 ± 0.35	−16.42 ± 2.76	8.0 ± 1.2	3.1 ± 0.5
Leo II	9	$0.48^{+0.03}_{-0.03}$	$0.368^{+0.002}_{-0.003}$	171 ± 2	465 ± 5	1.5 ± 0.1	0.7 ± 0.1	0.43 ± 0.04	0.87 ± 0.02	-1.30 ± 0.18	-5.49 ± 0.73	7.4 ± 1.3	4.5 ± 1.2
Ret2	9	$0.11^{+0.01}_{-0.01}$	$0.544^{+0.002}_{-0.002}$	55 ± 5	101 ± 9	1.0 ± 0.1	0.7 ± 0.1	0.03 ± 0.05	0.72 ± 0.02	-1.63 ± 0.40	−9.32 ± 1.30	3.1 ± 0.2	1.5 ± 0.2
Sextans	5	$0.81^{+0.05}_{-0.05}$	$0.553^{+0.017}_{-0.018}$	413 ± 3	747 ± 5	1.1 ± 0.1	0.7 ± 0.1	0.43 ± 0.04	1.00 ± 0.01	-0.08 ± 0.02	−3.42 ± 1.64	7.6 ± 2.1	4.7 ± 1.5
U Minor	5	$0.27^{+0.02}_{-0.01}$	$0.863^{+0.004}_{-0.007}$	407 ± 2	472 ± 2	1.0 ± 0.1	0.9 ± 0.1	0.11 ± 0.05	0.06 ± 0.05	−0.11 ± 0.19	0.02 ± 0.13	9.6 ± 1.9	9.9 ± 1.9

Table 2. The DM quantities derived in step III for both the Burkert profile (B) and the NFW profile. In column 8, 9 and 10, we show the mass at R_e (M_e) found from an equation derived in Ref. [14] (denoted as W09), the Burkert profile (B), and the NFW profile. The final three columns show the error in our models relative to the data (SD_{ret}) for the Burkert (B) and NFW profiles and the ratio of NFW/B uncertainties.

Galaxy	r_o/(pc)	r_s/(pc)	$\rho_0/(M_\odot pc^{-3})$	$\rho_s/(M_\odot pc^{-3})$	$M_0/(1e8M_\odot)$ (B)	$M_0/(1e8M_\odot)$ (NFW)	$M_e/(1e7M_\odot)$ (W09)	$M_e/(1e7M_\odot)$ (B)	$M_e/(1e7M_\odot)$ (NFW)	SD_{ret} (B)	SD_{ret} (NFW)	$\frac{SD_{ret}\ (NFW)}{SD_{ret}\ (B)}$
CVI	576 ± 52	883 ± 103	0.087 ± 0.019	0.037 ± 0.008	2.09 ± 1.02	2.62 ± 1.49	1.68	1.61 ± 0.79	2.18 ± 1.24	1.133	1.354	1.195
CVII	85.1 ± 8.5	104 ± 13	0.464 ± 0.035	0.315 ± 0.060	0.04 ± 0.02	0.04 ± 0.03	0.04	0.03 ± 0.02	0.05 ± 0.03	0.645	0.663	1.028
Draco	383 ± 35	547 ± 68	0.307 ± 0.044	0.095 ± 0.026	2.17 ± 0.74	1.97 ± 0.90	0.79	0.76 ± 0.26	0.96 ± 0.44	0.856	0.970	1.134
Fornax	1662 ± 151	2374 ± 297	0.020 ± 0.003	0.007 ± 0.002	11.35 ± 3.00	11.51 ± 5.58	4.11	3.09 ± 0.82	4.76 ± 2.18	0.523	1.149	2.198
Leo I	493 ± 38	328 ± 66	0.180 ± 0.020	0.227 ± 0.062	2.71 ± 0.76	1.01 ± 0.51	1.23	0.91 ± 0.26	1.50 ± 0.76	0.770	0.890	1.155
Leo II	310 ± 19	664 ± 83	0.358 ± 0.014	0.063 ± 0.016	1.34 ± 0.38	2.31 ± 1.15	0.65	0.46 ± 0.13	0.56 ± 0.28	0.806	1.129	1.401
Ret2	101 ± 9	144 ± 18	0.683 ± 0.095	0.214 ± 0.058	0.09 ± 0.02	0.08 ± 0.03	0.04	0.03 ± 0.01	0.04 ± 0.01	0.114	0.231	2.035
Sextans	679 ± 57	1068 ± 133	0.037 ± 0.004	0.016 ± 0.002	1.45 ± 0.62	2.38 ± 1.22	0.89	0.62 ± 0.27	1.14 ± 0.59	0.972	1.115	1.147
U Minor	471 ± 43	524 ± 52	0.135 ± 0.025	0.114 ± 0.020	1.78 ± 0.67	2.07 ± 0.77	2.22	1.67 ± 0.63	1.55 ± 0.58	0.992	0.973	0.980

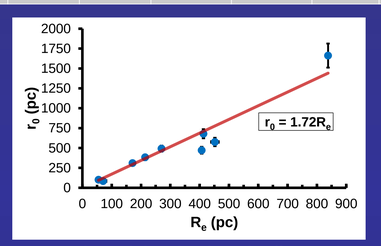

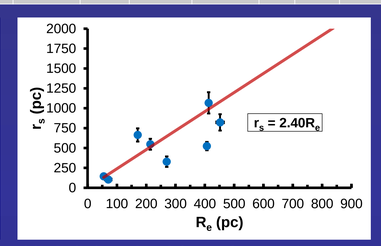

Figure 3. The DM halo scale radii vs. the effective radii (R_e) of the dSphs for Burkert (left, r_0) and NFW (right, r_s). In both graphs, the data points are blue dots and the best-fit curve is red.

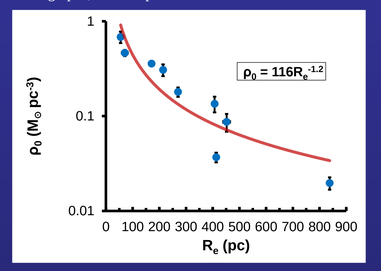

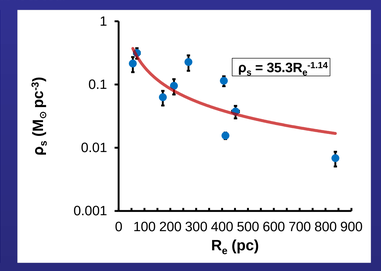

Figure 4. The DM halo density parameters vs. the effective radii (R_e) of the dSphs for Burkert (left, ρ_0) and NFW (right, ρ_s). In both graphs, the data points are blue dots and the best-fit curve is red.

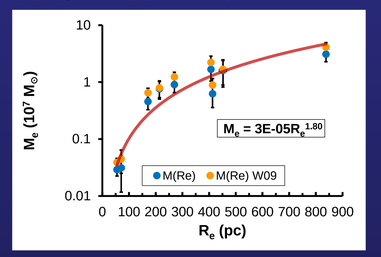

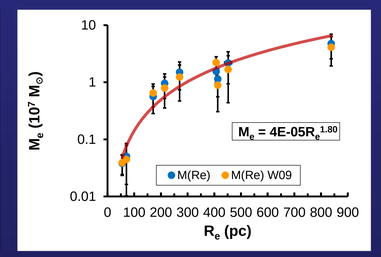

Figure 5. The total mass at the effective radius (M_e) of the dSphs for Burkert (left) and NFW (right). The blue dot are the data points from this analysis. The orange dots are estimates derived from Ref. [14] (denoted W09). The red trendline is the fit for the blue dots from this analysis.

Conclusions

In this work, we constrained the DM mass profiles and velocity anisotropy profiles of 9 MW dSphs. We draw four main conclusions:

1. A (cored) Burkert profile tends to describe the DM halos of MW dSphs more accurately than a (cuspy) NFW profile (Table 2).
2. The minimum uncertainty NFW model tends to require a large radial anisotropy near the origin (β_0~1) and an extremely tangential anisotropy at large r ($\beta_\infty < -3$), while the more accurate, minimum uncertainty Burkert models do not require such extremes (Table 2).
3. The DM halo parameters are highly correlated with the effective radius, R_e, for both Burkert and NFW models (Figs. 3 and 4).
4. NFW models tend to over-predict the mass at the effective radius, relative to previously published estimates [14], while Burkert models tend to under-predict it (Fig. 5).

References

[1] V. Trimble, ARA&A, 25, 425T (1987); M.Drewes et al. [arXiv:1602.04816 [hep-ph]].
[2] A. Brooks, Annalen Phys. 526 (7-8), 294 (2014) [arXiv:1407.7544 [astro-ph.CO]].
[3] P. A. R. Ade et al. [Planck Collaboration], Astron. Astrophys. 571, A16 (2014) [arXiv:1303.5076 [astro-ph.CO]].
[4] http://www-astro.physics.ox.ac.uk/~mxc/dark_matter_conspiracy.jpg
[5] http://chandra.as.utexas.edu/n4216-halo2.gif
[6] A. K. Vivas, M. Mateo, ApJ, 146 (6), 141 (2013) [arXiv:1309.2799v1 [astro-ph.SR]].
[7] A. G. Muskowitz, M.G. Walker, ApJ, 892 (2), 27 (2020) [arXiv:1910.10134 [astro-ph.GA]].
[8] N. Caldwell, et. al., ApJ, 839 (1), 20 (2016) [arXiv:1309.2799v1 [astro-ph.SR]].
[9] G. Torrealba, et al., MNRAS, 459 (3), 2370 (2016) [arXiv:1601.07178 [astro-ph.GA]].
[10] A. Geringer-Sameth, et al., ApJ, 801 (2), 74 (2015) [arXiv:1408.0002 [astro-ph.CO]].
[11] R. R. Munoz, et al., ApJ, 860, 65 (2018) [arXiv:1806.06891 [astro-ph.GA]].
[12] J. D. Simon, et al., (2015) [arXiv:1504.02889 [astro-ph.GA]].
[13] K. Bechtol, et al., [DES Collaboration], ApJ, 807 (1), 50 (2015) [arXiv:1503.02584 [astro-ph.GA]].
[14] M. G. Walker, et al., ApJ, 705 (2), 1274 (2009) [arXiv:0906.0341 [astro-ph.CO]].
[15] V. Bonnivard, et al., MNRAS, 808 (2), L36 (2015) [arXiv:1504.03309 [astro-ph.HE]].
[16] V. Bonnivard, et al., MNRAS, 446 (3), 3002 (2015) [arXiv:1407.7822 [astro-ph.HE]].
[17] H. C. Plummer, MNRAS, 71 (5), 460 (1911).
[18] J. H. Jeans, MNRAS, 76, 70 (1915).
[19] J. F. Navarro, et al., ApJ, 462, 563 (1996) [arXiv:astro-ph/9508025].
[20] A. Burkert, ApJ, 447, L25 (1995) [arXiv: astro-ph/9504041].